

Atomic Force Microscope-Based Meniscus-Confined Three-Dimensional Electrodeposition

David Eliyahu, Eliezer Gileadi, Ehud Galun, and Noam Eliaz*

The development of a 3D electrochemical deposition system, which combines meniscus-confined electrodeposition (MCED) with atomic force microscope (AFM) closed-loop control and has a submicron resolution, is described. Thanks to the high rigidity of the hollow borosilicate glass (or quartz) tip and quartz crystal tuning fork (QTF), combined with the QTF's high force sensitivity, the use of a solution-filled AFM tip in air is successful. The AFM control enables full automation and in situ growth control. Using this scheme, 3D printing of high-quality, fully dense, uniform and exceptionally smooth, freestanding straight and overhang pure polycrystalline copper pillars, with diameters ranging from 1.5 μm to 250 nm, and an aspect ratio > 100 , is demonstrated. This process may be useful for manufacturing of high-frequency terahertz antennas, high-density interconnects, precision sensors, micro- and nano-electromechanical systems, batteries, and fuel cells, as well as for repair or modification of existing micro-sized or nano-sized features.

1. Introduction

Several chemical and electrochemical microprinting methodologies were introduced over the years. Localized electrochemical deposition,^[1] for example, has been used to deposit mainly micropillars of copper or nickel with a resolution of a few microns, at best, high porosity, and poor surface finish.^[2–13] Nanotransfer printing has been used for forming 3D structures with feature sizes between tens of nanometers and tens of microns over areas of several square millimeters.^[14] Dip-pen nanolithography (DPN), first introduced by Mirkin et al.,^[15] is an atomic force microscope (AFM) tip based process that is used for transferring “ink” molecules (e.g., small organic molecules,

DNA, and metal ions) directly from the tip on to a surface.^[16–18] The combination of DPN and electrochemical deposition is the basis for electrochemical dip-pen nanolithography (E-DPN).^[19,20] In spite of its high resolution, E-DPN suffers from some significant limitations, such as very low deposition rate, limited amount of material on the tip, and no real three-dimensional (3D) capabilities. The electrochemical fabrication (EFAB) technology was invented by Cohen et al.^[21–24] as an improved LIGA process for mass production of microstructures with high aspect ratio and great structural height, based on combining lithography, electroplating, and plastic molding. The EFAB technology is capable of manufacturing metal devices, centimeters to millimeters in size, with micron-scale features as small as ca. 20 μm .

Electrochemical jet printing, also referred to as electrochemical printing, is a software reconfigurable tool and process for electrodeposition of multiscale, multimaterial objects from input drawings.^[25–27] A potential is applied between an anode assembled in a hollow micropipette and a cathode surface, while both the tip and the substrate are submerged in an electrolyte solution, thus locally electroplating individual metal and alloy dots.

Micro-channeled AFM tips have also been used.^[28–30] They allow fabrication of 3D metal structures with in situ control of the growth by the AFM control loop. The AFM hollow tips are marketed by Exaddon AG (formerly, Cytosurge AG, Glattbrugg, Switzerland) as FluidFM probes for certain commercial AFMs, or as part of its FluidFM μ3D printer.^[31] Controlling the voltage, flow rate, and stage motion, several 3D copper objects were fabricated layer-by-layer, having a width of several microns, an aspect ratio of up to 75, and angles as high as 90°, with a resolution of $\approx 1 \mu\text{m}$. In some cases, however, poor surface finish is evident.^[30]

The meniscus-confined electrodeposition (MCED) process, also known as electrochemical fountain pen nanofabrication, is an electrodeposition process that relies on an electrolyte-containing deposition tool (or electrolyte reservoir), typically in the form of a micropipette with a micron/submicron-size dispensing tip. When the micropipette approaches vertically the vicinity of a surface of a conductive substrate, a meniscus is established between the tip and the surface.^[32–48] Electrical potential (or current), applied between a small conductive wire inside the pipette and the conductive substrate via the meniscus, causes reduction of the reducible material on the surface confined by the meniscus. The dispensing micronozzle is then moved away from the substrate at a calibrated speed that matches

D. Eliyahu, Prof. N. Eliaz
Department of Materials Science and Engineering
Tel-Aviv University
Ramat Aviv, Tel Aviv 6997801, Israel
E-mail: neliaz@tau.ac.il

Prof. E. Gileadi
School of Chemistry
Tel-Aviv University
Ramat Aviv, Tel Aviv 6997801, Israel

Dr. E. Galun
Head of Materials Division
R&T Base Unit
DDR&D IMOD
Hakiryia, Tel Aviv 61909, Israel

 The ORCID identification number(s) for the author(s) of this article can be found under <https://doi.org/10.1002/admt.201900827>.

DOI: 10.1002/admt.201900827

the metal deposition speed in order to keep meniscus formation between the nozzle and the deposited materials, allowing continuous fabrication. Since the rate is affected by the nature of both the substrate and the solution, the pipette size, and the relative humidity (RH) percentage, new calibrations have to be done before every experiment. The feature size is influenced by several parameters, such as nozzle's diameter, its moving speed, the mechanical stability of the physical system (wettability), the thermodynamic properties of the electrolyte solution, and the environment/electrodeposit/substrate interfaces. The majority of the substrate can be kept out of the solution (which can in certain cases be harmful), and no masks or sacrificial layers are required. Using the MCED process, the ability to create straight and overhang pillars as well as precise electrical connections has been demonstrated. Several metals, including Cu, Pt, Co, Ni, and Au, have been successfully employed in MCED to fabricate micro- and nanostructures. Other conducting materials, such as polyaniline, have also been deposited. MCED has been claimed to be an appealing alternative for future printing of solid oxide fuel cells, even compared to stereolithography and extrusion.^[49] Yet, in some cases the reported structures suffer from high porosity, poor surface finish, and other flaws.^[34,35,43,45,48] More information on electrochemical printing processes as well as on nanoelectrochemistry using micro- and nano-electrodes or pipettes is summarized elsewhere.^[50,51]

In all prior technologies described above, the tip motion is at predefined speed and direction that are determined based on preliminary experiments of growth speed and applied current. However, many factors affect the deposition rate, including the solution and substrate in use, the actual orifice of the pipette, and the RH. For example, a nonuniform substrate is sufficient to change the deposition rate from one point to another, resulting in a nonuniform printing. Here, the development of a 3D electrochemical deposition system that combines MCED with AFM closed-loop control (e.g., in the form of a quartz crystal tuning fork [QTF], i.e., resonance control) and has a submicron resolution^[52] is described. Owing to the closed-loop control, also known as feedback control, either the substrate or the tip is retracted away from the deposition front, in a speed equal to the printing rate, thus maintaining a constant distance between the tip and the printed feature. Thus, full automation and in situ growth control are enabled, rendering unnecessary the need for trial-and-error preliminary experiments, and resulting in a much more uniform deposition, which is less affected by the substrate or solution properties. Thanks to the high rigidity of the hollow borosilicate glass (or quartz) tip and QTF, combined with the QTF's high force sensitivity, the use of a solution-filled AFM tip in air is successful. Using this scheme, 3D printing of freestanding, high-quality, dense, and exceptionally smooth, straight and angled pure copper pillars of different sizes and high aspect ratios is demonstrated. The main differences between the new MCED system and prior art are discussed in the Supporting Information Materials and Methods.

2. Results and Discussion

The feedback control needs to be sensitive, stable, and of fast response. Three types of feedback control were studied:

beam bounce, lateral tuning fork (LTF), and normal tuning fork (NTF).^[52] The latter yielded the best results and will only be demonstrated hereafter. Selected results obtained using beam bounce and LTF controls and the shortcomings of these controls are included in the Supporting Information Results and in Figure S1, Supporting Information. NTF (tapping mode) exhibited high sensitivity in the vertical direction, fast response, a constant motion speed, a stable voltage/current, and high repeatability.

The distance between the tip orifice and the substrate is important because it affects the deposition rate and structure due to different evaporation rates,^[47] as well as the deposit diameter. In our setup, the tip is in a high and constant proximity to the surface (a few tens of nanometers according to the tip amplitude measurements) thanks to the closed-loop feedback. Moreover, only negligible changes can be made to the set point, limiting the range of possible tip-to-surface distance to only a few tens of nanometers. Consequently, while the deposition rate can only be controlled by current density, the printed item exhibits a uniform and smooth surface.

Figure S2, Supporting Information, shows the effect of applied current on the shape and surface morphology of printed Cu pillars. As the cathodic current is increased, the surface of the printed pillar becomes finer due to grain size refinement.^[53] However, at sufficiently high cathodic overpotential (namely, more negative than ca. -1.4 V), hydrogen evolution interrupts Cu deposition and causes a less uniform surface. The finest pillars were obtained when applying a cathodic current between -4 and -5 nA (for a micropipette with a $1\ \mu\text{m}$ orifice diameter). Figure S2, Supporting Information, reveals that the diameter of the printed Cu pillars ($\approx 1.5\ \mu\text{m}$) is larger than the orifice diameter of the micropipette, and that the base of the pillar is even larger. Regarding the first phenomenon, it has been reported that a small tip-to-substrate distance combined with a 1:2 inner-to-outer tip diameters ratio cause the formation of larger meniscus, and as a result, a larger deposition area.^[47] Similarly, the larger base size can be attributed to a small tip-to-substrate distance and approach speed, as well as to the hydrophilic nature of Cu.^[54]

Figure 1 shows a) the potential transient, b) side view, and c) top view of a freestanding straight Cu pillar that was printed galvanostatically ($I = -5$ nA) using an NTF feedback control and a $1\ \mu\text{m}$ micropipette. The pillar is uniform, fully dense with almost no porosity visible, and exceptionally smooth (compare to the surface finish of the substrate—a pure Cu foil polished down to $40\ \text{nm}$ colloidal silica). These are important advantages of electrochemical 3D printing over conventional metal additive manufacturing (AM) technologies such as powder bed fusion (PBF) and directed energy deposition (DED). The quality of the pillar is also higher than in most previous publications dealing with electrochemical microprinting (see the aforementioned literature survey). The oval shape of the cross-section results from the oval shape of the tip opening of this specific micropipette. Figure 1d,e shows scanning electron microscope (SEM) images of Cu pillars printed at $I = -1.5$ nA from a micropipette with an orifice diameter of $400\ \text{nm}$. The actual diameter of the printed pillar is larger ($\approx 500\ \text{nm}$), as explained before. Note that the pillars do not bend, and that they have high aspect ratios (e.g., a height-to-diameter ratio of 40 in Figure 1e). Figure 1f

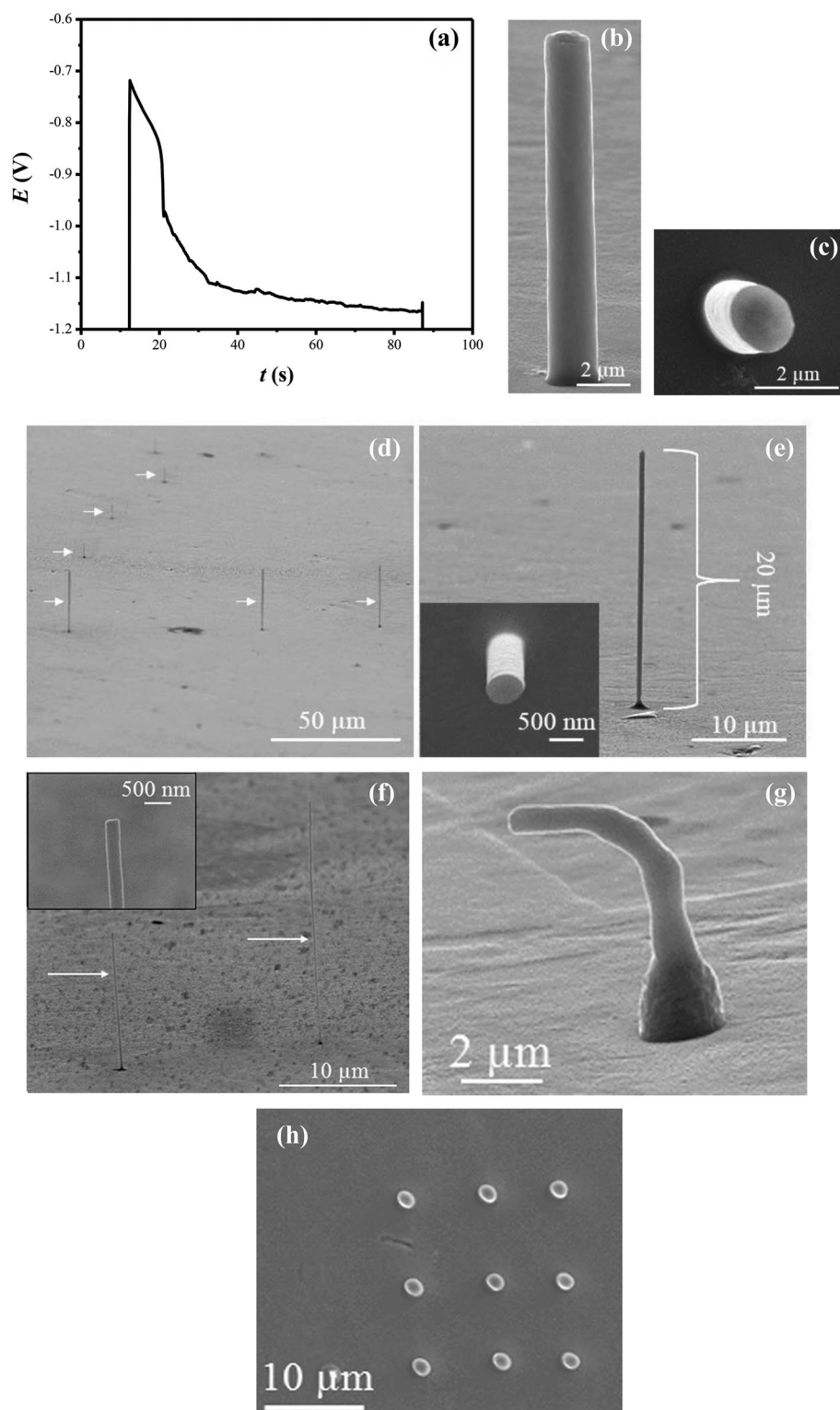


Figure 1. a) Potential transient during galvanostatic printing ($I = -5$ nA) of a Cu pillar from a micropipette with an inner diameter of $1 \mu\text{m}$. b) SEM side image of the self-supported straight pillar from a) on a polished Cu foil substrate. Note the uniformity and fine surface finish. c) SEM top view of the same pillar. Note the high density and lack of evident defects. d and e) SEM images of Cu pillars printed at $I = -1.5$ nA from a micropipette with an inner diameter of 400 nm. f) SEM image of two Cu pillars printed at $I = -400$ pA from a micropipette with an inner diameter of 100 nm. The inset shows a zoom-in image of the upper part of one pillar. g) SEM image of an angled pillar printed with a $1 \mu\text{m}$ tip and a constant lateral movement speed of 400 nm s^{-1} , resulting in an overhang angle of 80° . Lateral motion started after 1 min of vertical printing. h) Automatic printing of a 3×3 matrix of $1.5 \mu\text{m}$ pillars. Deposition current: -5 nA.

Table 1. The effects of the micropipette inner diameter on the printed Cu pillar diameter, deposition current, deposition current density, and average deposition rate.

Pipette size [μm]	Pillar diameter [μm]	Current, I [nA]	Current density [mA cm^{-2}]	Average deposition rate [nm s^{-1}]
1	1.5	5	283	90
1	1.5	6	340	105
0.4	0.55	1	421	160
0.4	0.61	1.2	411	130
0.1	0.23	0.3	722	300
0.1	0.27	0.4	699	230

shows an SEM image of two Cu pillars printed at $I = -400$ pA from a micropipette with an orifice diameter of 100 nm. The actual diameter of the printed pillar is larger (≈ 250 nm). Using such pipettes, aspect ratios >100 were achieved. It should be noted that the height of the printed pillars is limited by the piezo range of motion in the positive z -direction, which is ≈ 30 μm in our system. This limitation can easily be overcome using other available piezo stages. The high-aspect-ratio structure does not deflect or buckle under its own weight (i.e., the pillars are relatively stiff compared with their own weight) because on small length scales, body forces are relatively ineffective at deforming structures compared to surface forces.^[55] Furthermore, experiments on micro- and nano-electromechanical systems (M/NEMS) have shown that their behavior under bending loads departs in many cases from the classical predictions using the Euler–Bernoulli theory and Hooke’s law. The residual stress, couple stress, grain boundary, surface elasticity, and surface stress theories have been suggested to explain such size dependence.^[56]

The relations between the pipette size, the actual diameter of the printed pillar, the applied current, the applied current density, and the average deposition rate are summarized in **Table 1**. As the pipette orifice diameter is reduced, both the printed pillar diameter and the associated deposition current decrease, whereas the current density and the related deposition rate increase. For a smaller-sized meniscus, it was found that a higher current density can be applied while avoiding hydrogen evolution, probably as a result of a higher evaporation rate from the meniscus surface that causes higher mass transport within it. The effect of mass transport within a small capillary on the measured current density was discussed before (see, for example, ref. [46]). It was found that diffusion by itself cannot explain the high current density that is achieved in the MCD process. Only by adding the contribution of migration, and especially convection due to water evaporation, is a better understanding of the mass transport obtained. The maximum deposition rate we have monitored is 300 nm s^{-1} ($1080 \text{ } \mu\text{m h}^{-1}$). This deposition rate is sufficiently high for many industrial applications.

One could ask whether the amplitude of the tuning fork oscillation influences the electroplating process, and might the oscillations induce convective mass transport in the capillary. To answer these questions, we should first bear in mind that amplitude measurements indicated that the distance between the tip and the substrate was around 20 nm. This distance may

change a little bit from tip to tip as well as by the user input. It is reasonable to assume that the oscillation does not affect the deposition owing to its relatively small amplitude and high frequency. While the tip orifice retracts at a speed of 300 nm s^{-1} , the tuning fork oscillates at a frequency of 36 kHz, i.e., at a much higher movement speed. For the above values of amplitude and frequency, the linear velocity in the z -direction is

$$v = 2\pi \times 36000 \times 20 \times 10^{-9} = 0.0045 \text{ ms}^{-1} \quad (1)$$

i.e., a three orders of magnitude higher than the tip motion. The implication of this value is that the tip can be treated as static.

Because of the small tip diameter, the fluid in it is very viscous and can be considered to behave as a solid, tracking the pipette movement. The fluid resistance to flow can be represented by a small Reynolds number, $\text{Re} \ll 1$, which reflects a Stokes flow regime. Calculating the Reynolds number and considering the maximum velocity of the fluid that can be attained with an orifice diameter of 1 μm , one gets

$$\text{Re} = \frac{0.0045 \text{ ms}^{-1} \times 10^{-6} \text{ m}}{8.92 \times 10^{-7} \text{ m}^2 \text{ s}^{-1}} = 0.005 \quad (2)$$

The Stokes number can be calculated from

$$\text{Stk} = \frac{t_0 \times u_0}{l_0} \quad (3)$$

where t_0 is the droplet relaxation time, u_0 is the tip velocity, and l_0 is the orifice diameter.

In the case of Stokes flow:

$$t_0 = \frac{\rho_p \times d_p^2}{18\mu_g} \quad (4)$$

where ρ_p is the droplet density, d_p is the droplet diameter, and μ_g is the gas dynamic viscosity (or, the glass viscosity). Substituting the following values for water at 22 °C: $\rho_p = 997 \text{ kg m}^{-3}$, $\mu_g = 8.9 \times 10^{-4} \text{ kg m}^{-1} \text{ s}^{-1}$, $d_p = 10^{-6} \text{ m}$, one gets $\text{Stk} = 0.005$. This is a very small value, implying that the fluid moves as one unit with the tip. Since the deposition rate in this study is similar to that in previous studies, it may be concluded that the tuning fork oscillations do not induce convective mass transport in the capillary.

In order to study the capability to print hanging structures, a designated feature in the AFM software was exploited. Deposition of angled pillars took place by a combined vertical–lateral motion, namely keeping the closed-loop control “on” and adding a horizontal movement in a predefined speed and path. Figure 1g presents a structure deposited in one continuous motion with a lateral constant movement speed of 400 nm s^{-1} . The resulting overhang angle is 80° . As the lateral speed is decreased from 400 to 100 nm s^{-1} , the overhang angle decreases from 80° to 40° . Lateral speeds higher than 400 nm s^{-1} caused the meniscus to break. Owing to the meniscus shape, it is more difficult to maintain a steady connection while moving horizontally, especially as there is no closed-loop control that corrects the tip position. It should be noted that one of the advantages of

electrochemical 3D printing could be the ability to manufacture items with overhang angles higher than 45° from the vertical, which is usually regarded as the threshold value above which supports are needed in PBF processes. Finally, the automatic printing of a series of structures is demonstrated in Figure 1h. This 3×3 matrix of $1.5 \mu\text{m}$ Cu pillars was programmed via the NWS software, the applied current was -5 nA .

Next, material characterization of printed pillars is reported. Two transverse cross-sections were extracted using a focused ion beam (FIB)-SEM and are compared here: a) $4 \mu\text{m}$ thick extracted from a $1.5 \mu\text{m}$ in diameter pillar, and b) 70 nm thick extracted from a 500 nm in diameter pillar. Figure 2a is a SEM image of a). A fully dense cross-section is evident, with almost no detectable pores. This conclusion is supported by calculation of the theoretical height of the printed structure. Energy dispersive X-ray spectroscopy (EDS) analysis not shown here indicates chemical composition of pure Cu (Pt peaks are also evident, but they are related to sample preparation). Figure 2b is a SEM image of b). A fully dense cross-section of pure Cu is observed in this case too. The presence of extinction contours inside many grains in bright-field images of a scanning transmission electron microscope (STEM), not shown herein, could indicate high internal stresses. STEM electron diffraction reveals a rings pattern (Figure 2c) that can be indexed according to the lattice planes characteristic of face centered cubic (fcc) Cu. No preferred orientation is evident in the z -direction. Transmission electron backscatter diffraction (t-EBSD) analysis of transverse cross-section b) also shows no preferred orientation (Figure 2d) as well as grain size of $62 \pm 24 \text{ nm}$ ($n = 45$). Measuring the average grain size manually, using the Heyn lineal intercept procedure,^[57] gives a similar value of $49 \pm 3 \text{ nm}$. In comparison, the corresponding value for the larger cross-section a) is much higher: $158 \pm 13 \text{ nm}$. The larger grain size can be attributed to the lower deposition current density ($282 \text{ vs } 500 \text{ mA cm}^{-2}$). Substituting $\sigma_0 = 40 \text{ MPa}$ and $k = 0.11 \text{ MPa m}^{1/2}$ into the Hall–Petch relationship,^[58] we estimate the yield strength of Cu in the $1.5 \mu\text{m}$ and 500 nm pillars to be 317 and 537 MPa , respectively. For comparison, copper C11000 has yield strength of 76 MPa in the annealed condition and 324 MPa in the extra hard (H06) condition, whereas a yield stress of 390 MPa was measured for submicron-grained Cu.^[59] The high strength of the as-printed Cu pillars may thus be attributed to their submicron grain size.

Since materials printed with technologies such as PBF and DED are often not uniform in the z -direction (mainly, due to thermal effects), a longitudinal cross-section of a $20 \mu\text{m}$ high, 500 nm in diameter, printed pillar was also characterized. It is evident (Figure 2e) that the material is fully dense, and that there is some change in the grain size from the central axis of the pillar (where it is smaller) to the surface (where it is larger). The second characteristic could result either from higher ion concentration at the liquid/solid interphase, which causes larger grain growth,^[60] or from recrystallization at the pillars surface over time, which is typical of nanocrystalline Cu structures at ambient conditions as a result of the high energy stored.^[61,62] Since no grain growth was observed near the circumference of the transverse cross-sections that were stored for shorter times before FIB-SEM characterization, we believe that recrystallization is more likely the cause of this grain growth

in this work. Both SEM and t-EBSD measurements yield grain size of $85 \pm 25 \text{ nm}$ ($n = 58$), i.e., significantly larger than in the transverse cross-section. This may indicate a nonequiaxed grain structure. As shown in Figure 1e,g and discussed above, the base of the printed pillar is of larger diameter. The grains in this zone are also larger, which can be related to less cathodic deposition potential/current density (see Figure 1a) and, hence, lower nucleation rates and higher grain growth rates.

Measurement of the electrical resistivity of the printed Cu features is of interest for many applications. In addition, high electrical conductivity of the as-printed feature could indicate on a fully dense material, with a low concentration of defects such as impurities and defected interfaces between printed layers. The assembly for four-point probe measurements is shown in Figure S3, Supporting Information. The potential versus current plot for a 500 nm in diameter, $\approx 20 \mu\text{m}$ long pillar (Figure 2f) reveals an Ohmic behavior (i.e., metallic nature) with a slope of 4.01Ω . The average resistivity is $3.15 \times 10^{-7} \Omega \text{ m}$, an order of magnitude higher than pure bulk oxygen-free high copper in its annealed condition at 20°C , $(1.71\text{--}2.46) \times 10^{-8} \Omega \text{ m}$ (70–101% IACS).^[63,64] This, however, may be related to the Pt contact resistance (that generates heat) rather than to an inherent property of printed Cu. A dense pure Cu processed via selective electron beam melting, for comparison, has been reported to have an electrical conductivity $\sigma = 5.582 \times 10^7 \text{ S m}^{-1}$ ($\rho = 1.79 \times 10^{-8} \Omega \text{ m}$), based on eddy current measurements.^[65] Nevertheless, our measured resistivity is similar to that reported for nano-grained Cu pillars,^[66] and could thus be related to electron scattering by high density of grain boundaries. In addition, our measured value is slightly lower than $3.9 \times 10^{-7} \Omega \text{ m}$ reported for nanotwinned Cu produced by localized pulsed electrodeposition (L-PED).^[48] PED (or higher current densities) can be used to obtain a structure of high-density nanoscale twins, which exhibits superior mechanical and electrical properties compared to coarse-grained and nano-grained structures.^[48,67]

Electrochemical AM methods have some distinct potential advantages compared to powder-base and other AM technologies: 1) They have the ability to reach a submicron resolution; 2) in contrast to conventional AM, in 3D electrochemical printing the subject may be deposited without any heating, thus no heat-affected zone (HAZ)-related phenomena exist, residual stresses are minimal, no subsequent annealing or homogenization heat treatment is required, and the material is more uniform along the z -axis; 3) support structures can be eliminated; 4) a fine surface roughness may be achieved, thus no complementing surface polishing processes are required; 5) the chemicals and reagents are typically cheaper; 6) the equipment is cheaper, smaller, and simpler to operate; 7) no use of small reactive powders or high power lasers, therefore less safety concerns. The solutions are often safer to transport and handle; 8) less recycling limitations; and 9) materials that are hard to print in good quality by common AM technologies such as PBF or DED, such as Li, Mg, and Al, may be easier to print, e.g., using nonaqueous media such as organic solvents, molten salts, or ionic liquids. Conducting polymers can similarly be printed.^[52] The method developed herein may be used for fabricating nanowires, high-density interconnects for integrated circuits, direct writing of submicron scale circuitry for

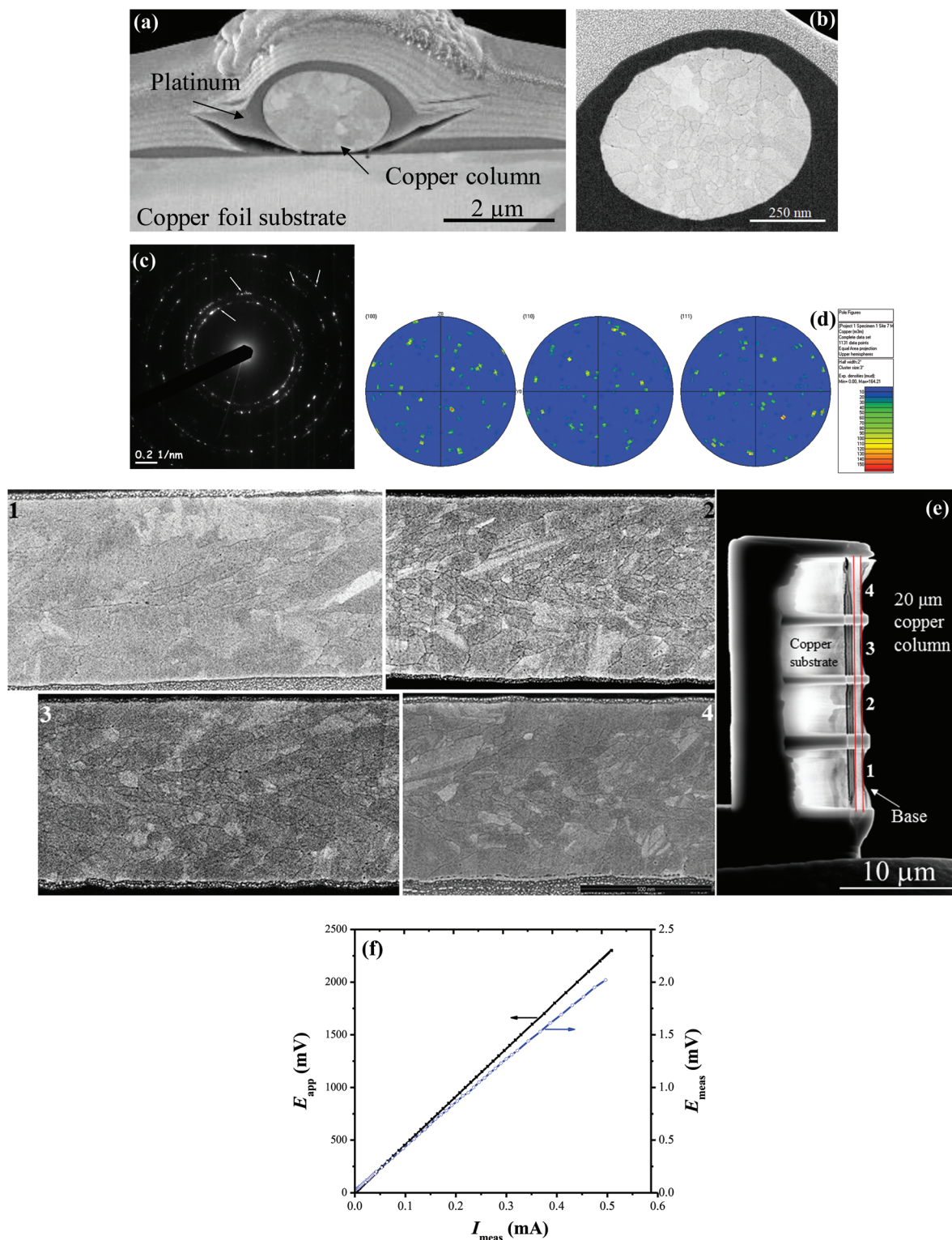


Figure 2. a) SEM image of the cross-section extracted by FIB-SEM from of a 1.5 μm printed Cu pillar. b) SEM image of the cross-section extracted by FIB-SEM from of a 500 nm printed Cu pillar. c) STEM electron diffraction pattern of (b). The four diffraction rings match, from inside outside, the (111), (200), (220), and (311) lattice planes of fcc Cu. d) t-EBSD inverse pole figure, z-direction coloring scheme, from the transverse cross-section of a 500 nm in diameter Cu pillar. e) Longitudinal cross-section from a 500 nm in diameter, 20 μm high printed Cu pillar. On the right is a STEM image of the pillar, divided to four parts in order to avoid collapse. Corresponding SEM images of the four parts are shown on the left. f) Four-point probe plot drawing the applied and measured potentials (left and right ordinates, black and blue graphs, respectively) versus the measured current. A linear, Ohmic behavior is evident. For the measured potential: slope = 4.01 Ω , $R^2 = 0.99964$. For the applied potential: slope = 4.54 Ω , $R^2 = 0.99998$.

advanced display technologies and advanced electronic packaging, conductive bridges and precise electrical connections, thermocouples, interposers, high-frequency terahertz antennas, probe arrays, precision sensors, N/MEMS, batteries, and fuel cells. In addition, it may be used to repair or modify existing micro-sized or nano-sized features; it is perfectly situated to tackle the issue of yield enhancement by local printing of sub-micron to few microns missing conductive tracks.

3. Conclusion

In summary, we developed an electrochemical microprinting system with submicron resolution, which combines MCED with AFM closed-loop control.^[52] Three types of feedback control were compared: beam bounce, LTF and NTF, the latter giving the best results. The AFM control enables full automation and in situ growth control. This methodology enables to print in air, i.e., to avoid immersion of the whole substrate in a solution. As a proof of concept, we 3D printed various structures from pure Cu. Suitable deposition potential/current and RH conditions for printing pure Cu were first determined. Hollow borosilicate glass pipettes with orifice diameters of 1 μm , 400, and 100 nm were used, thus obtaining printed pillars with diameters of 1.5 μm , 500, and 250 nm, respectively, and aspect ratios higher than 100. A significant deposition rate of 300 nm s⁻¹ was monitored. High-quality, fully dense, uniform, and exceptionally smooth, freestanding straight, overhang, and array pillars were printed. Overhang angles as high as 80° were achieved without using any supports. The printed pillars were characterized as having a submicron-grained microstructure with no preferred orientation, exceptionally high strength, low electrical resistivity, and Ohmic behavior. Future improvement of the new microprinting system could include the addition of a multi-axis piezo stage, high-precision micropump, a lateral closed-loop control, and movement of the printing head. In principal, any material that can be electrodeposited can also be 3D printed using the new microprinting

system. Such materials include metals, alloys, conducting polymers, semiconductors, ceramic suspensions, metallic glasses, functionally graded materials (FGMs), and composites. Printing of multimaterials could also be possible, using multiple micropipettes, while the adaptation to electroless deposition will allow printing on nonconductive substrates.

4. Experimental Section

Microprinting System: As a proof of concept, the system was constructed around an AFM (Multiview 1000, Nanonics, Jerusalem, Israel). The AFM was controlled via a LabVIEW-based designated software (NWS, Nanonics, Jerusalem, Israel). The AFM piezo motor had a range of 80 μm in the *x* and *y* axes, and 65 μm in the *z*-axis. The RH affected the wettability properties of the surfaces as well as the evaporation rate of water from the liquid bridge,^[46] which both influenced the quality of the printed item. Therefore, the AFM was positioned inside an acoustic chamber (PicoIC, Molecular Imaging, Phoenix, AZ, USA), which served as an environment chamber, maintaining constant RH of 60–70%. The RH percentage was regulated by passing air through a flask containing water directly to the chamber. The humidity inside the chamber was monitored with a thermohygrometer (608-H1, Testo, Lenzkirch, Germany), while the flow control was done manually. The environment chamber was positioned on an anti-vibration table (78-227-12R/CleanTop II, TMC/Ametek, PA, USA). The printed pillars were too small for in situ optical monitoring. However, an optical objective lens (zoom 6000, Navitar, New York, USA) with a 3.2-megapixel digital camera (ColorView 2, Olympus, Tokyo, Japan) was mounted above the tip in order to monitor its position in a continuous manner. Illustration of the microprinting system is given in **Figure 3a**.

Micropipettes: For successful printing, the system should have high sensitivity to forces applied on the tip, fast response, and rigid structure. The tip cantilever should not deflect due to the weight of the solution or the surface tension force (snap on/off). A hollow glass AFM tip connected to the bottom cantilever of a tuning fork and working in tapping mode with phase feedback was found to meet all operational requirements. Specially designed AFM tips (Nanonics, Jerusalem, Israel) with pipette orifice diameters of 1 μm , 400, and 100 nm were used. The origin borosilicate glass or quartz tubes were heated and pulled using a laser puller (P-2000, Sutter, CA, USA). Beam-bounce tips were coated

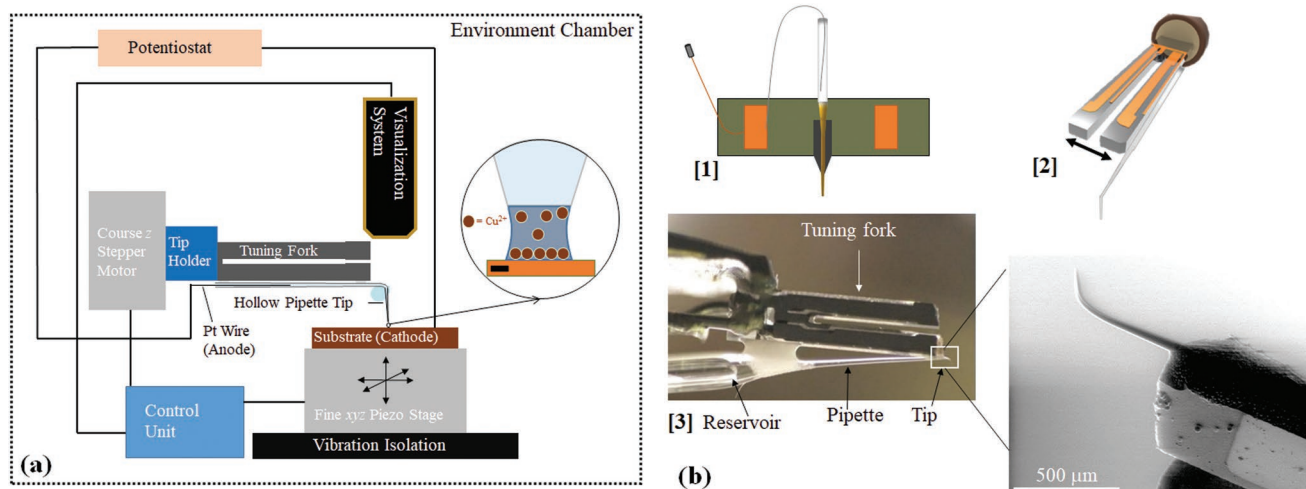


Figure 3. a) Schematics of the innovative AFM-MCED microprinting system. The inset shows a zoom-in of the substrate-meniscus-pipette apex zone. b) Three types of hollow AFM tips: 1) Illustration of a beam-bounce tip glued to a magnetic holder. A gold coating is applied by CVD from the cantilever nearly all the way to the tip end. A platinum wire is inserted through the backside. 2) Illustration of an LTF in which the pipette is attached to the TF on its side. 3) An image of an NTF in which the pipette is attached to the bottom cantilever of the TF.

with Au by chemical vapor deposition (CVD) and glued to a magnetic holder, while tips with TF were connected through a UV glue both to the TF and to a special adapter. When the TF was connected perpendicular to the ground, the pipette is connected beneath it, facing down, and the tip is referred to as NTF. In contrast, when connected horizontally, the pipette is attached to it from the side, and the tip is referred to as a LTF tip (Figure 3b). The final tips had a cantilever length of 100–1000 μm , a backside opening of 500 μm , a ratio of 2:1 between their external and inner diameters, a high spring constant ($k > 20 \text{ N m}^{-1}$), and a resonance frequency of around 34.2 kHz (with TF feedback).

Operation Principle: The substrate was positioned on top of the piezo driver, which retracted the tip according to the feedback loop. A course stepper motor brought the tip to an initial connection with the substrate. A platinum wire was inserted to the back of the tip and was connected together with the conductive substrate to a SourceMeter. The printing began when the tip approached the substrate while current was applied. When a connection was recognized and a liquid meniscus was formed, the tip was stopped by the AFM closed-loop control. At this point, a closed electrical circuit was established (as evident from a sharp change in potential/current), and reduction of the metal ions was initiated, confined to the meniscus area. While deposition continues in the vertical direction, the force applied on the tip changes. As a result of a change in the tuning fork, signal was recognized, and an in situ correction of tip-substrate distance took place by the AFM closed-loop control. As deposition continued, the tip-to-substrate distance changed at the same rate, maintaining a constant meniscus shape and uniform cross-section. The liquid bridge (i.e., meniscus) formed by dispensing an electrolyte solution from the micropipette tip onto the surface had a diameter that substantially equaled the inner diameter of the tip, and a height defined by the distance between the substrate surface or a site of further deposition (in a sequential off-substrate deposition step) and the tip.

The Substrate and the Two-Electrode Electrochemical Cell Configuration: A two-electrode configuration was used. The counter electrode was either a 25 or 50 μm in diameter 99.99% pure platinum wire (GoodFellow, Huntingdon, England). Because the highest applied currents were of the order of only few nanoamperes, the polarization of the platinum wire can be assumed negligible, and it can be regarded as a *pseudo* reference electrode.^[68] The substrate (working electrode) was 675 μm thick, 99.9% pure copper foil (Alfa-Aesar, MA, USA). The foil was first ground with SiC papers, from 240P down to 2400P. Next, it was polished with a 1 μm diamond suspension, followed by 40 nm colloidal silica suspension. Then, it was rinsed with water, placed in a chemical glass with deionized water, sonicated for 5 min, rinsed again with water, rinsed with ethanol, and dried with cold blowing air. After electrochemical printing, the substrate was cleaned with a droplet of ethanol and dried again. A current (or potential) was applied between a platinum wire and a copper foil substrate using a SourceMeter (2450-EC Electrochemistry Lab System, Keithley, Beaverton, Oregon, USA). The SourceMeter was controlled via a freeware software (KickStart, Tektronix, Beaverton, Oregon, USA). A potential of ca. -1.0 V (vs Pt) was found to give good deposition rate while avoiding hydrogen evolution, which might cause instability of the meniscus.

The Electrolyte Solution for Printing Pure Copper: The acidic (pH 1) aqueous electrolyte solution for electrochemical printing consisted of 50 mM $\text{CuSO}_4 \cdot 5\text{H}_2\text{O}$ (copper (II) sulfate pentahydrate, 99%, Alfa-Aesar, MA, USA), and 50 mM H_2SO_4 (sulfuric acid, 95.0–98.0%, Sigma-Aldrich, MO, USA). The salt concentration was chosen to enable the highest deposition rate while preventing tip clogging as a result of salt recrystallization.^[38] Before inserting to the pipette, the solution was filtered through a 0.2 μm syringe filter (Minisart, Sartorius, Göttingen, Germany), in order to prevent clogging by large particles. When using micropipettes with an orifice smaller than 500 nm in diameter, the solution was filtered through a 100 kDa centrifugal filter (Amicon Ultra-4, Merck, NJ, USA).

Characterization of the Printed Cu Pillars: High-resolution secondary and backscattered electrons images were acquired using a SEM (Quanta 200 FEG ESEM, FEI, MA, USA). The chemical composition of the printed

pillars was determined by EDS (INCA detector, Oxford Instruments, Abington, UK) integrated in the SEM system. Samples for EDS were prepared by FIB microscope (Helios NanoLab 600 DualBeam, FEI, MA, USA) down to a thickness of several microns, and were kept in a desiccator until characterization. Samples prepared by FIB and placed on a TEM copper grid were used for t-EBSD (also known as transmission Kikuchi diffraction, TKD) characterization inside the SEM. Images were processed with a designated software (AZtecHKL, Oxford Instruments, Abington, UK). Grain size distribution was obtained from t-EBSD data, and was compared to manual calculation from SEM images, using the Heyn Lineal Intercept Procedure.^[57] Bright-field and dark-field images as well as electron diffraction patterns were acquired using a STEM (JEM 2010F, JEOL, Tokyo, Japan). Samples for STEM characterization were prepared in a FIB microscope, down to a thickness of 70 nm. The STEM images were processed with a Digital Micrograph software (Gatan, Pleasanton, CA, USA). Electrical resistivity measurements were conducted on pillars 500 nm in diameter and $\approx 20 \mu\text{m}$ long. A silicon wafer with a 600 nm silicon oxide (SiO_2) layer was used as the substrate in four-point probe measurements. Four 50 nm thick gold pads were deposited onto the wafer by lithography. The Cu pillars were positioned on the substrate inside the FIB microscope, and were connected to the gold pads by platinum wires, as shown in Figure S3, Supporting Information. Electrical measurements were conducted in ambient environment, using a four-probe station (Janis, Woburn, MA, USA). In a dual-channel SourceMeter (2603B, Keithley, Cleveland, OH, USA), the two inner probes were connected to one SMU, while the outer probes to the second one. A potential was applied between the two outer pads, and the current was measured. Potential was measured on the inner connections, eliminating the effect of contact resistance. To prevent excessive heating due to the relatively high resistance of the Pt connections, each potential was measured separately, for a short period of time.

Supporting Information

Supporting Information is available from the Wiley Online Library or from the author.

Acknowledgements

The authors gratefully acknowledge the financial support from the Israel Ministry of Defense (grant no. 4440783376). The authors thank Dr. Zahava Barkay and Dr. George Levi from the Wolfson Applied Materials Research Center as well as Dr. Eran Granot from the Center for Nanoscience and Nanotechnology at Tel-Aviv University for their assistance with t-EBSD, TEM, and electrical resistivity measurements, respectively. The technical assistance of Mr. Mario Levinshtein is also acknowledged. The authors would also like to acknowledge the thoughtful discussions with Professors Shachar Richter, Arie Ruzin, Amit Kohn, Slava Krylov, and Herman Haustein.

Conflict of Interest

The authors declare no conflict of interest.

Keywords

atomic force microscope (AFM), copper, electrochemistry, meniscus-confined electrodeposition (MCED), three-dimensional (3D) printing

Received: September 18, 2019

Revised: December 10, 2019

Published online: January 9, 2020

- [1] J. D. Madden, I. W. Hunter, *J. Microelectromech. Syst.* **1996**, 5, 24.
- [2] A. Jansson, G. Thornell, S. Johansson, *J. Electrochem. Soc.* **2000**, 147, 1810.
- [3] E. M. El-Giar, R. A. Said, G. E. Bridges, D. J. Thomson, *J. Electrochem. Soc.* **2000**, 147, 586.
- [4] S. H. Yeo, J. H. Choo, *J. Micromech. Microeng.* **2001**, 11, 435.
- [5] R. A. Said, *Nanotechnology* **2004**, 15, 867.
- [6] S. K. Seol, A. R. Pyun, Y. Hwu, G. Margaritondo, J. H. Je, *Adv. Funct. Mater.* **2005**, 15, 934.
- [7] J. C. Lin, S. B. Jang, D. L. Lee, C. C. Chen, P. C. Yeh, T. K. Chang, J. H. Yang, *J. Micromech. Microeng.* **2005**, 15, 2405.
- [8] C. S. Lin, C. Y. Lee, J. H. Yang, Y. S. Huang, *Electrochem. Solid-State Lett.* **2005**, 8, C125.
- [9] J. C. Lin, J. H. Yang, T. K. Chang, S. B. Jang, *Electrochim. Acta* **2009**, 54, 5703.
- [10] J. C. Lin, T. K. Chang, J. H. Yang, Y. S. Chen, C. L. Chuang, *Electrochim. Acta* **2010**, 55, 1888.
- [11] A. M. Brant, M. M. Sundaram, A. B. Kamaraj, *J. Manuf. Sci. Eng.* **2015**, 137, 011018.
- [12] M. M. Sundaram, A. B. Kamaraj, V. S. Kumar, *J. Manuf. Sci. Eng.* **2015**, 137, 021006.
- [13] F. Wang, H. Xiao, H. He, *Sci. Rep.* **2016**, 6, 26270.
- [14] J. Zaumseil, M. A. Meitl, J. W. P. Hsu, B. R. Acharya, K. W. Baldwin, Y.-L. Loo, J. A. Rogers, *Nano Lett.* **2003**, 3, 1223.
- [15] R. D. Piner, J. Zhu, F. Xu, S. Hong, C. A. Mirkin, *Science* **1999**, 283, 661.
- [16] J. Jang, G. C. Schatz, M. A. Ratner, *Phys. Rev. Lett.* **2003**, 90, 156104.
- [17] D. S. Ginger, H. Zhang, C. A. Mirkin, *Angew. Chem., Int. Ed.* **2004**, 43, 30.
- [18] K. Salaita, Y. Wang, C. A. Mirkin, *Nat. Nanotechnol.* **2007**, 2, 145.
- [19] Y. Li, B. W. Maynor, J. Liu, *J. Am. Chem. Soc.* **2001**, 123, 2105.
- [20] H. Kang, S. Hwang, J. Kwak, *Nanoscale* **2015**, 7, 994.
- [21] A. L. Cohen, U. Frodis, F. G. Tseng, G. Zhang, F. Mansfeld, P. M. Will, in *Proc. SPIE 3874, Micromachining and Microfabrication Process Technology V* (Eds. J. H. Smith, J. M. Karam) **1999**, p. 236.
- [22] A. Cohen, G. Zhang, F. G. Tseng, U. Frodis, F. Mansfeld, P. Will, in *Proc. MEMS'99: 12th IEEE Int. Conf. on Micro Electro Mechanical Systems* **1999**, p. 244.
- [23] A. Cohen, White paper, Microfabrica Inc., Burbank **2005**.
- [24] Microfabrica, Inc., <http://microfabrica.com/> (accessed: December 2019).
- [25] J. D. Whitaker, J. B. Nelson, D. T. Schwartz, *J. Micromech. Microeng.* **2005**, 15, 1498.
- [26] J. B. Nelson, Z. Wisecarver, D. T. Schwartz, *J. Micromech. Microeng.* **2007**, 17, 1192.
- [27] J. B. Nelson, D. T. Schwartz, *J. Electrochem. Soc.* **2008**, 155, D181.
- [28] A. Meister, M. Liley, J. Brugger, R. Pugin, H. Heinzelmann, *Appl. Phys. Lett.* **2004**, 85, 6260.
- [29] A. Meister, M. Gabi, P. Behr, P. Studer, J. Vörös, P. Niedermann, J. Bitterli, J. Polesel-Maris, M. Liley, H. Heinzelmann, T. Zambelli, *Nano Lett.* **2009**, 9, 2501.
- [30] L. Hirt, S. Ihle, Z. Pan, L. Dorwling-Carter, A. Reiser, J. M. Wheeler, R. Spolenak, J. Vörös, T. Zambelli, *Adv. Mater.* **2016**, 28, 2311.
- [31] Exaddon AG, <https://www.exaddon.com/> (accessed: December 2019).
- [32] J. Jang, G. C. Schatz, M. A. Ratner, *Phys. Rev. Lett.* **2004**, 92, 085504.
- [33] K. H. Kim, N. Moldovan, H. D. Espinosa, *Small* **2005**, 1, 632.
- [34] T. Leïchlé, L. Nicu, E. Descamps, B. Corso, P. Mailley, T. Livache, C. Bergaud, *Appl. Phys. Lett.* **2006**, 88, 254108.
- [35] A. P. Suryavanshi, M.-F. Yu, *Appl. Phys. Lett.* **2006**, 88, 083103.
- [36] R. C. Major, J. E. Houston, M. J. McGrath, J. I. Siepmann, X.-Y. Zhu, *Phys. Rev. Lett.* **2006**, 96, 177803.
- [37] A. Fang, E. Dujardin, T. Ondarçuhu, *Nano Lett.* **2006**, 6, 2368.
- [38] A. P. Suryavanshi, M. F. Yu, *Nanotechnology* **2007**, 18, 105305.
- [39] J. Hu, M.-F. Yu, *Science* **2010**, 329, 313.
- [40] K. McKelvey, M. A. O'Connell, P. R. Unwin, *Chem. Commun.* **2013**, 49, 2986.
- [41] B. C. Gross, J. L. Erkal, S. Y. Lockwood, C. Chen, D. M. Spence, *Anal. Chem.* **2014**, 86, 3240.
- [42] R. D. Farahani, K. Chizari, D. Therriault, *Nanoscale* **2014**, 6, 10470.
- [43] S. K. Seol, D. Kim, S. Lee, J. H. Kim, W. S. Chang, J. T. Kim, *Small* **2015**, 11, 3896.
- [44] Z. Yi1, J. Guo, Y. Chen, H. Zhang, S. Zhang, G. Xu, M. Yu, P. Cui, *Microsyst. Nanoeng.* **2016**, 2, 16010.
- [45] D. Momotenko, A. Page, M. Adobes-Vidal, P. R. Unwin, *ACS Nano* **2016**, 10, 8871.
- [46] S. Morsali, S. Daryadel, Z. Zhou, A. Behroozfar, D. Qian, M. Minary-Jolandan, *J. Appl. Phys.* **2017**, 121, 024903.
- [47] S. Morsali, S. Daryadel, Z. Zhou, A. Behroozfar, M. Baniyasi, S. Moreno, D. Qian, M. Minary-Jolandan, *J. Appl. Phys.* **2017**, 121, 214305.
- [48] A. Behroozfar, S. Daryadel, S. R. Morsali, S. Moreno, M. Baniyasi, R. A. Bernal, M. Minary-Jolandan, *Adv. Mater.* **2018**, 30, 1705107.
- [49] J. C. Ruiz-Morales, A. Tarancón, J. Canales-Vázquez, J. Méndez-Ramos, L. Hernández-Afonso, P. Acosta-Mora, J. R. Marín Rueda, R. Fernández-González, *Energy Environ. Sci.* **2017**, 10, 846.
- [50] N. Eliaz, E. Gileadi, *Physical Electrochemistry: Fundamentals, Techniques, and Applications*, 2nd ed. (Eds: E. Gileadi, N. Eliaz), Wiley-VCH, Weinheim, Germany **2019**, p. 372.
- [51] C. Ru, J. Luo, S. Xie, Y. Sun, *J. Micromech. Microeng.* **2014**, 24, 053001.
- [52] D. Eliyahu, N. Eliaz, E. Gileadi, (Tel-Aviv University), *International Patent Application PCT/IL2019/051110*, October 10, **2019**.
- [53] N. D. Nikolić, K. I. Popov, L. J. Pavlović, M. G. Pavlović, *J. Electroanal. Chem.* **2006**, 588, 88.
- [54] H. Ghasemi, C. A. Ward, *J. Phys. Chem. C* **2010**, 114, 5088.
- [55] J. A. Pelesko, D. H. Bernstein, *Modeling MEMS and NEMS*, Chapman & Hall/CRC, Boca Raton, FL **2003**, pp. 65–75.
- [56] A. M. Abazari, S. M. Safavi, G. Rezazadeh, L. G. Villanueva, *Sensors* **2015**, 15, 28543.
- [57] ASTM E112 – 12, *Standard Test Methods for Determining Average Grain Size*, American Society for Testing and Materials, West Conshohocken, PA **2012**.
- [58] Z. C. Cordero, B. E. Knight, C. A. Schuh, *Int. Mater. Rev.* **2016**, 61, 495.
- [59] R. Z. Valiev, E. V. Kozlov, Y. F. Ivanov, J. Lian, A. A. Nazarov, B. Baudelet, *Acta Metall. Mater.* **1994**, 42, 2467.
- [60] D. Grujicic, B. Pesic, *Electrochim. Acta* **2002**, 47, 2901.
- [61] S. H. Brongersma, E. Richard, I. Vervoort, H. Bender, W. Vandervorst, S. Lagrange, G. Beyer, K. Maex, *J. Appl. Phys.* **1999**, 86, 3642.
- [62] V. Y. Gertsman, R. Birringer, *Scr. Metall. Mater.* **1994**, 30, 577.
- [63] D. Chapman, *High Conductivity Copper for Electrical Engineering*, Copper Development Association, Hemel Hempstead, UK, **2016**.
- [64] The Copper Advantage: A Guide to Working with Copper and Copper Alloys, https://www.copper.org/publications/pub_list/pdf/a1360.pdf (accessed: December 2019).
- [65] S. J. Raab, R. Guschlbauer, M. A. Lodes, C. Körner, *Adv. Eng. Mater.* **2016**, 18, 1661.
- [66] W. Gu, K. Kim, in *2006 IEEE Nanotechnology Materials and Devices Conf.*, IEEE, Gyeongju, South Korea **2006**, pp. 304–305.
- [67] L. Lu, Y. Shen, X. Chen, L. Qian, K. Lu, *Science* **2004**, 304, 422.
- [68] (Eds.: G. Inzelt, A. Lewenstam, F. Scholz), *Handbook of Reference Electrodes*, Springer-Verlag, Berlin Heidelberg **2013**.